Engineering 51 (2025) 240–253

Contents lists available at ScienceDirect

Engineering

journal homepage: www.elsevier.com/locate/eng

Research
Hydraulic Engineering—Article

Modelling of Flood Risks to People's Life and Property in the Lower Yellow River Under Different Floodplain Management Modes

Yifei Cheng [a], Junqiang Xia [a,*], Hongwei Fang [b,c], Meirong Zhou [a], Zuhao Zhou [d], Jun Lu [e], Dongyang Li [f], Roger A. Falconer [g,h], Yuchuan Bai [i]

[a] State Key Laboratory of Water Resources Engineering and Management, Wuhan University, Wuhan 430072, China
[b] State Key Laboratory Hydroscience and Engineering, Tsinghua University, Beijing 100084, China
[c] Department of Ocean Science and Engineering, Southern University of Science and Technology, Shenzhen 518055, China
[d] State Key Laboratory of Simulation and Regulation of Water Cycle in River Basins, China Institute of Water Resources and Hydropower Research, Beijing 10048, China
[e] Yellow River Engineering Consulting Co., Ltd., Zhengzhou 450000, China
[f] Henan Yellow River Engineering Consulting Co., Ltd., Zhengzhou 450000, China
[g] Hydro-environmental Research Centre, School of Engineering, Cardiff University, Cardiff CF24 3AA, UK
[h] Yangtze Institute Conservation and Development, Hohai University, Nanjing 210024, China
[i] State Key Laboratory Hydraulic Engineering Intelligent Construction, Tianjin University, Tianjin 300350, China

ARTICLE INFO

Article history:
Received 19 February 2024
Revised 24 May 2024
Accepted 24 February 2025
Available online 26 February 2025

Keywords:
Integrated modelling
People's life and property
Flood risk evaluation
Floodplain management modes
Lower Yellow River

ABSTRACT

Quantification of river flood risks is a prerequisite for floodplain management and development. The lower Yellow River (LYR) is characterized by a complex channel–floodplain system, which is prone to flooding but inhabits a large population on the floodplains. Many floodplain management modes have been presented, but implementation effects of these management modes have not been evaluated correctly. An integrated model was first proposed to evaluate the flood risks to people's life and property, covering an improved module of two-dimensional (2D) morphodynamic processes and a module of flood risk evaluation for people, buildings and crops on the floodplains. Two simulation cases were then conducted to validate the model accuracy, including the hyperconcentrated flood event and dike-breach induced flood event occurring in the LYR. Finally, the integrated model was applied to key floodplains in the LYR, and the effects of different floodplain management modes were quantified on the risks to people's life and property under an extreme flood event. Results indicate that: ① Satisfactory accuracy was achieved in the simulation of these two flood events. The maximum sediment concentration was just underestimated by 9%, and the simulated inundation depth agreed well with the field record; ② severe inundation was predicted to occur in most domains under the current topography (Scheme I), which would be alleviated after implementing different floodplain management modes, with the area in slight inundation degree accounting for a large proportion under the mode of "construction of protection embankment" (Scheme II) and the area in medium inundation degree occupying a high ratio under the mode of "floodplain partition harnessing" (Scheme III); and ③ compared with Scheme I, the high-risk area for people's life and property would reduce by 21%–49% under Scheme II, and by 35%–93% under Scheme III.

1. Introduction

River flooding is one of the most common and frequent natural disasters, and causes devastating consequences in human society and ecological environments [1–3]. It is reported that global river floods result in direct economic losses exceeding one trillion dollars and more than 0.2 million fatalities during the period 1980–2013 [4,5]. Flood damages are predicted to accumulate in the future, due to the increase in flood frequency induced by extreme climate changes and the steady growth in population and economic activities in flood-prone areas over the world, including the densely populated basin of the lower Yellow River

* Corresponding author.
E-mail address: xiajq@whu.edu.cn (J. Xia).

https://doi.org/10.1016/j.eng.2025.02.011

(LYR) [6–9]. Estimations of flood risks to people's life and property in these areas are imperative to implement effective management strategies, for which accurate modelling of flood inundation processes is a prerequisite [10,11].

Commonly, there are two methods to quantify the flood inundation extent, including numerical modelling and satellite observations. Although interpretation from satellite images can currently provide efficient estimates of inundated areas [12–14], it fails to reveal the dynamics of flooding such as the variations in water depth and flow velocity. Therefore, the method of numerical modelling is widely used to simulate the flood inundation processes. Due to the computational cost and numerical instability, three-dimensional (3D) models are impractical in the simulation for large rivers [11]. To date, two-dimensional (2D) models are the most useful tool to simulate the flood routing processes for large rivers especially those with complex channel–floodplain systems.

Most existing 2D morphodynamic models are proposed for the simulation of routing processes of floods with very low sediment concentrations [15–17]. Because the influences of sediment concentration and bed evolution are neglected on flood routing in these models, they are merely capable to simulate the morphodynamic processes associated with low sediment concentrations and bed deformation rates [18–21]. For the rivers with heavy sediment load such as the LYR, the flows often carry high sediment concentrations during flood seasons, with the value of sediment concentration more than 200 $kg{\cdot}m^{-3}$ recorded. Some 2D coupled morphodynamic models can simulate the flow-sediment transport processes at laboratory scales or generalized channel boundaries [20,22–23], but they are not tested in real-world settings. For example, Yue et al. [20] proposed a 2D well-balanced, coupled morphodynamic model based on unstructured grids with efficient variable storage strategy, and validated the model using some laboratory experiments. Therefore, it is necessary to develop a 2D coupled model, in order to simulate the complex morphodynamic processes induced by highly sediment-laden floods over the irregular topography of the LYR.

Once the flood inundation processes and corresponding hydrodynamic parameters are obtained, a flood risk evaluation can be conducted based on a property-by-property assessment. The losses of human and economy covering people, buildings, and crops are discussed herein, which are closely related to flooding indicators such as water depth and flow velocity in the view of mechanical analysis. Many formulas or criteria have been proposed for the stability of a human body in floodwater based on experimental data or mechanical analyses [24,25]. Currently, a new criterion is widely accepted for the stability of a human body in floodwater in the form of an incipient velocity proposed by Xia et al. [25], based on a mechanics-based analysis accounting for the effect of body buoyancy and the influence of a non-uniform velocity profile acting on the flooded human body. This criterion has been integrated into some 2D hydrodynamic models to assess the flood risk to people during urban floods or river floods [26–28], which has not yet been adopted in the LYR with a complex channel–floodplain system. Previous studies [29–30] of flood losses of buildings and crops usually focus on the depth-damage curves, which are determined through field surveys. However, more mechanical analyses and adequate field surveys should be made when assessing the flood losses of buildings and crops in a specific catchment.

The LYR basin is uniquely composed of main channel and vast floodplains, and the latter accounts for more than 70% of the total basin area. These floodplains in the LYR occupy an area of 4000 km^2, which are currently populated 1.5 million people. But these domains are flood-prone zones, which are consistently disturbed by floods caused by extreme climate changes. In addition, the phenomenon of "secondary perched river" extensively exists in the braided reach of the LYR, which can exacerbate the degree of overbank flooding. According to the historical record, around 31 overbank flooding events occurred in the LYR during the period 1949–2018, with more than 9 million people affected [3]. As a consequence, the contradiction becomes more inevitable between flood control and economic development in these domains. Although many floodplain management modes have been put forward for the LYR, there is a lack of effective modelling techniques and appropriate risk evaluation methods to discuss the effects of different governance strategies in previous studies. Therefore, the aims of the current study are to: ① propose an integrated model for morphodynamic process simulation and flood risk evaluation; ② validate the integrated model in real-world settings, by simulating the hyperconcentrated flood event and dike-breach induced flood event occurring in the LYR; and ③ quantify the effects of different floodplain management modes, by applying the model to evaluate the flood risks to people's life and property under an extreme flood event with a 1000-year return period.

2. Description of the integrated model

The integrated model consists of two modules, covering a module of 2D morphodynamic process and a module of flood risk evaluation. The improved 2D morphodynamic module is specially designed for the LYR with a complex channel–floodplain system and hyperconcentrated floods. The module of flood risk evaluation can calculate the hazard degrees of main flooded objects on the floodplains, covering people, buildings, and crops.

2.1. Module of 2D morphodynamic processes

The modified hydrodynamic governing equations of the 2D morphodynamic module consist of the mass and momentum conservation equations for the sediment-laden flows, which can be written as [20,22,31]:

$$\frac{\partial \boldsymbol{U}}{\partial t}+\frac{\partial \boldsymbol{E}}{\partial x}+\frac{\partial \boldsymbol{G}}{\partial y}=\boldsymbol{R} \tag{1}$$

$$\rho'\frac{\Delta Z_{b,k}}{\Delta t}=\alpha_{s,k}\omega_{s,k}(S_k-S_{*,k}) \tag{2}$$

where $\boldsymbol{U}$ is the vector of conserved variables; $\boldsymbol{E}$ and $\boldsymbol{G}$ are the convective fluxes along the x and y global coordinates, respectively; $\boldsymbol{R}$ is the source term, including the bed slope terms, friction slope terms, and additional terms arisen by sediment transport and bed deformation; t denotes the time; ρ' is the dry density of bed material; k is the kth sediment fraction; $\Delta Z_{b,k}$ is the thickness of bed deformation caused by the kth sediment fraction during a time step of Δt; S_k and $S_{*,k}$ are the concentration and transport capacity for the kth sediment fraction, respectively; $\omega_{s,k}$ and $\alpha_{s,k}$ are the settling velocity and recovery coefficient of the kth sediment fraction. The vectors in Eq. (1) are written in detail as follows:

$$\boldsymbol{U}=\begin{bmatrix} h \\ hu \\ hv \\ hS_k \end{bmatrix},\ \boldsymbol{E}=\begin{bmatrix} hu \\ hu^2+\frac{1}{2}gh^2 \\ huv \\ huS_k \end{bmatrix},\ \boldsymbol{G}=\begin{bmatrix} hv \\ huv \\ hv^2+\frac{1}{2}gh^2 \\ hvS_k \end{bmatrix},$$
$$\boldsymbol{R}=\underbrace{\begin{bmatrix} 0 \\ gh(T_{b,x}-T_{f,x}) \\ gh(T_{b,y}-T_{f,y}) \\ -\alpha_{s,k}\omega_{s,k}(S_k-S_{*,k}) \end{bmatrix}}_{\mathrm{I}}+\underbrace{\begin{bmatrix} -\partial Z_b/\partial t \\ -\frac{\Delta\rho g h^2}{2\rho_m\rho_s}\frac{\partial S}{\partial x}+\left(\frac{\rho_b-\rho_m}{\rho_m}\right)u\frac{\partial Z_b}{\partial t} \\ -\frac{\Delta\rho g h^2}{2\rho_m\rho_s}\frac{\partial S}{\partial y}+\left(\frac{\rho_b-\rho_m}{\rho_m}\right)v\frac{\partial Z_b}{\partial t} \\ 0 \end{bmatrix}}_{\mathrm{II}} \tag{3}$$

where h is the average water depth of a computational cell; u and v denote components of the depth-averaged flow velocity along the x and y coordinates; g is gravitational acceleration; $T_{b,x}$ and $T_{b,y}$ are

the components of the bed slope term (T_b) along the x and y coordinates, with $T_{b,x} = -\frac{\partial Z_b}{\partial x}$ and $T_{b,y} = -\frac{\partial Z_b}{\partial y}$; Z_b is riverbed elevation; $T_{f,x}$ and $T_{f,y}$ are the components of the friction slope term (T_f) along the x and y coordinates, with $T_{f,x} = n^2 u\sqrt{u^2+v^2}h^{-\frac{4}{3}}$ and $T_{f,y} = n^2 v\sqrt{u^2+v^2}h^{-\frac{4}{3}}$; n is Manning's roughness coefficient; $\Delta\rho = \rho_s - \rho_w$, where ρ_s is sediment density and ρ_w is clear water density; $\rho_b = (1-\rho'/\rho_s)\rho_w + \rho'$ is the density of saturated bed material; $\rho_m = S + (1-S/\rho_s)\rho_w$ is the density of sediment-laden flow; S is the total concentration of graded sediments. The second part II in $\boldsymbol{R}$ is the key of the coupled solution, which represents the effects of the spatial variations of sediment concentration and bed deformation on flow momentum. These additional terms can be neglected using the uncoupled solution when simulating low-concentrated flows, which however exert a great effect on the transport processes of hyperconcentrated floods or the floods associated with rapid channel evolution rates.

The finite volume method is well conserved and commonly used in previous studies. It is adopted to solve the governing equations based on unstructured meshes, which are able to reflect irregular channel geometries in natural rivers. All the conserved variables are stored in the cell centroid, and the edge of a cell defines the interface between this cell and its neighboring cell. In the current module, the Harten–Lax–van Leer (HLL)-monotone upstream centered scheme for conservation laws (MUSCLs) scheme is adopted to compute flow and sediment fluxes through the interface. The detailed discretization of hydrodynamic equations including the calculation of some source terms are presented in Appendix A. The details of model parameters, reconstruction of digital terrain, and grid generation process are also presented in Appendix A.

2.2. Module of flood risk evaluation

Flood risk evaluation involves the estimation of adverse effects of flooding on people's life and property in the inundated area, and the corresponding evaluation indicators commonly include the inundation extent, duration, economic loss, and affected population [3–5]. The module of flood risk evaluation is specially proposed to calculate the flood hazard degrees of people's life and property on the floodplains. Agricultural economy dominates in the floodplains of the LYR, among which crop farming is the most important. The floods usually occur during the period from July to September in the LYR, when the summer grains (e.g., wheat and barley) have been harvested but the autumn grains (e.g., corn and cotton) are in growth. It has been investigated that the planting area of corn is the largest among the autumn grains [3]. Therefore, three flooded objects covering people, buildings, and corn are considered in the module of flood risk evaluation, with the detailed calculation relations described as follows.

2.2.1. Calculation of flood hazard degree of people

Two types of method to assess the human body stability were used in previous studies, including regressed relations based on a number of laboratory experimental studies using real human bodies and semi-theoretical formulas derived from a mechanics-based analysis [24]. Both criteria show some limitations. The former was significantly dependent on the physical attributes and psychological factors of the test objects, while the latter made excessive simplification on the human body structure and flow condition [25]. Xia et al. [25] made an improved study on the criterion of people stability in floodwaters, which can overcome these limitations. In order to derive this criterion, different forces acting on a human body were analyzed, including the body buoyancy and the drag force, with the influence of a non-uniform velocity profile being considered (Fig. 1). Then the corresponding formulas of incipient velocity were deduced based on the instability mechanisms for the modes of sliding and toppling. Because the mode of sliding instability usually occurs for flows with shallow depths and high flow velocities, only the formula for toppling instability is adopted in this study. When a person stands facing the oncoming flow direction, as shown in Fig. 1, the critical condition for toppling instability is that the human body would pivot around the heel (point O) and topple backwards as the total moment around the pivot point O is equal to zero. The formula of incipient velocity for toppling instability (U_c) can be written as:

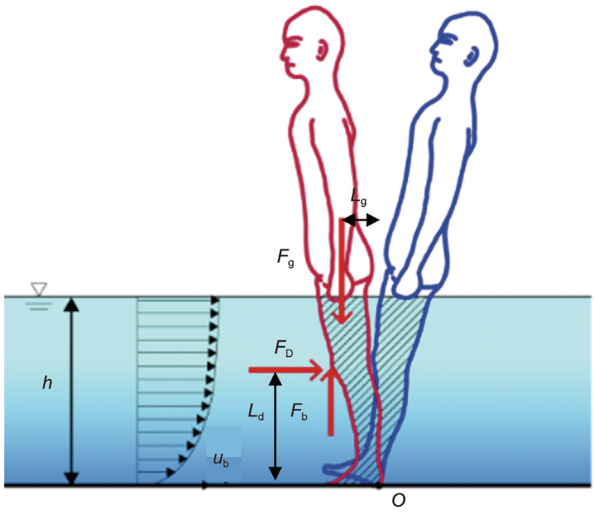

Fig. 1. Sketch of the forces acting on a flooded human body for toppling instability [25]. F_D: drag force; F_b: buoyancy force; F_g: gravitational force; L_d, L_g: moment arms of the drag force and effective weight; u_b: representative near-bed velocity.

$$U_c = \beta_1\left(\frac{h}{h_p}\right)^{\beta_2} \times\sqrt{\frac{m_p}{\rho_m h^2} - \left(\frac{0.633}{h_p^2}+\frac{0.367}{h\cdot h_p}\right)\left(1.015\times10^{-3}m_p - 4.927\times10^{-3}\right)} \tag{4}$$

where h_p and m_p are the average height and weight of an adult, which is assumed to be 1.7 m and 60 kg in the study; and β_1 and β_2 are comprehensive parameters. Details about this formula can be found in Ref. [25]. After calibrated by measurements, the proposed formula is able to accurately identify the stability threshold, which represents the state of the art in this field, as commended by Milanesi et al. [32] and Chanson and Brown [33]. Then the flood hazard degree of people (HD_{people}) is calculated by:

$$HD_{people} = \min(U/U_c, 1.0) \tag{5}$$

where U is the average velocity of a computational cell, m·s^{-1}; HD_{people} is an indicator of the probability of toppling instability for an adult in floodwater. If the value of HD_{people} is close to 1.0, an adult will be more likely to topple in the flow.

2.2.2. Calculation of flood hazard degree of buildings

Analyses of flood damage to buildings often focus on the effect of inundation depth, with the depth-damage curves developed in previous studies [34,35]. The importance of flooding parameters other than water depth was also discussed in some studies [36,37]. Kelman [37] made a full analysis of flood forces acting on a building with hydrostatic and hydrodynamic actions considered, and the forces acting on a building are illustrated in Fig. 2(a). The lateral pressure imparted by the water flowing around a building is related to water depth and flow velocity,

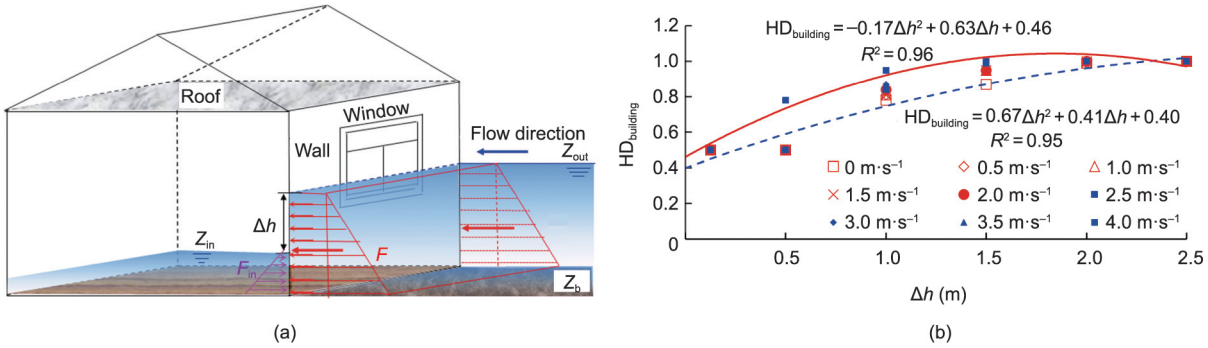

Fig. 2. (a) Sketch of the forces acting on a building; (b) fitting curves for hazard degree. Z_{in}: water level inside a building; Z_{out}: water level outside a building; F: force of flowing water; F_{in}: hydrostatic pressure; R^2: determination coefficient; $HD_{building}$: loss rate of a building in floodwater; Δh: difference of water depth inside and outside a building.

which consequently are the main factors to cause damage to buildings. After some field surveys to determine characteristics of the physical vulnerability of buildings, Kelman [37] concluded a risk matrix in different combinations of the difference of water depth inside and outside a building and flow velocity, which can be fitted by the curves (Fig. 2(b)) and written as:

$$HD_{building}\begin{cases}(-17\Delta h^2+63\Delta h+46)/100 & U=4\,m\cdot s^{-1}\\(-23\Delta h^2+41\Delta h+40)/100 & U=0\,m\cdot s^{-1}\end{cases} \quad (6)$$

where the value of $HD_{building}$ being equal to 1.0 indicates that a building is completely ruined. It should be noted that the hazard degree is interpolated in correspondence to other combinations of water depth and flow velocity based on Eq. (6).

2.2.3. Calculation of flood hazard degree of crop

The damage to corn during flood seasons is the main rural damage in the floodplains of the LYR. Corn is a temperature-loving crop, the growth and quality of which will be influenced by excessive water. Existing studies have acknowledged that inundation depth and duration are main factors to cause damage to corn [30,38]. Geomorphic changes and sediment concentrations also have impacts on the growth of crops [3,39,40]. However, there is a lack of field surveys about the relationship between the loss of corn and geomorphic changes. Therefore, it is still reasonable to establish a relationship between the loss of corn and inundation depth and duration based on field surveys of real flood events, which can indirectly reflect the influences of sediment concentrations and geomorphic changes during a flood event. Based on the field surveys of damage to corn in previous studies [38], a power relation can be established to calculate the flood hazard degree of corn (Fig. 3):

$$HD_{corn} = 0.48h^{0.35}T_{in}^{0.34} \quad (7)$$

where T_{in} is the inundation duration; and HD_{corn} represents the loss rate of corn induced by a flood. The larger the value of HD_{corn} is, the greater damage is. Based on Eqs. (5)–(7), the flood hazard degree of each object in a floodplain cell can be calculated. The flow velocity will be very close to the incipient velocity of toppling instability for an adult when the hazard degree reaches 0.85 [38], which suggests an extreme danger. As a consequence, the level of high risk is defined with the value of hazard degree larger than 0.85 in the current study.

It should be noted that the scales of a specified flood object and a computation cell are not always reconciled. It is impossible to plot a grid which only accommodates a human body or a building. Therefore, the hazard degree of each flooded object is calculated based on the land use types in the study area. After the land use types including town and cropland are determined, the hazard degree of each object is calculated cell by cell. For example, the hazard degree for buildings is calculated over the computation cells which are labeled as a town. People will be present in all the cells except the main channel zone, and consequently the hazard degree is calculated across these cells, utilizing the average velocity of a computation cell as the flow velocity within the relevant formula [41]. Based on this treatment, the calculation of hazard degree in the study area is reconciled with the proposed formulas.

3. Validation of the integrated model

Three types of data were used in the current study for validation and flood risk evaluation in the following section. The first category focuses on topography, encompassing both routine cross-sectional profile surveys, such as those conducted at the Jiahetan (JHT) section in Henan Province and the Gaocun (GC) section in Shandong Province (Fig. 4(a)), and irregular floodplain topography using Autodesk computer-aided design (CAD) maps. Seven hydrometric stations, namely Huayuankou (HYK), JHT, GC, Sunkou (SK), Aishan (AS), Luokou (LK), and Lijin (LJ), are set up (Fig. 4(a)). The first two stations are situated in Henan Province, while the remaining five are located in Shandong Province. The second type pertains to

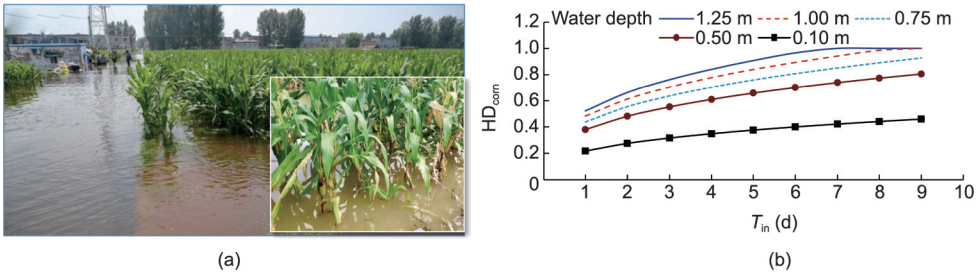

Fig. 3. Estimation of corn loss. (a) The inundated corn in a floodplain; (b) relationship between hazard degree and inundation duration and depth.

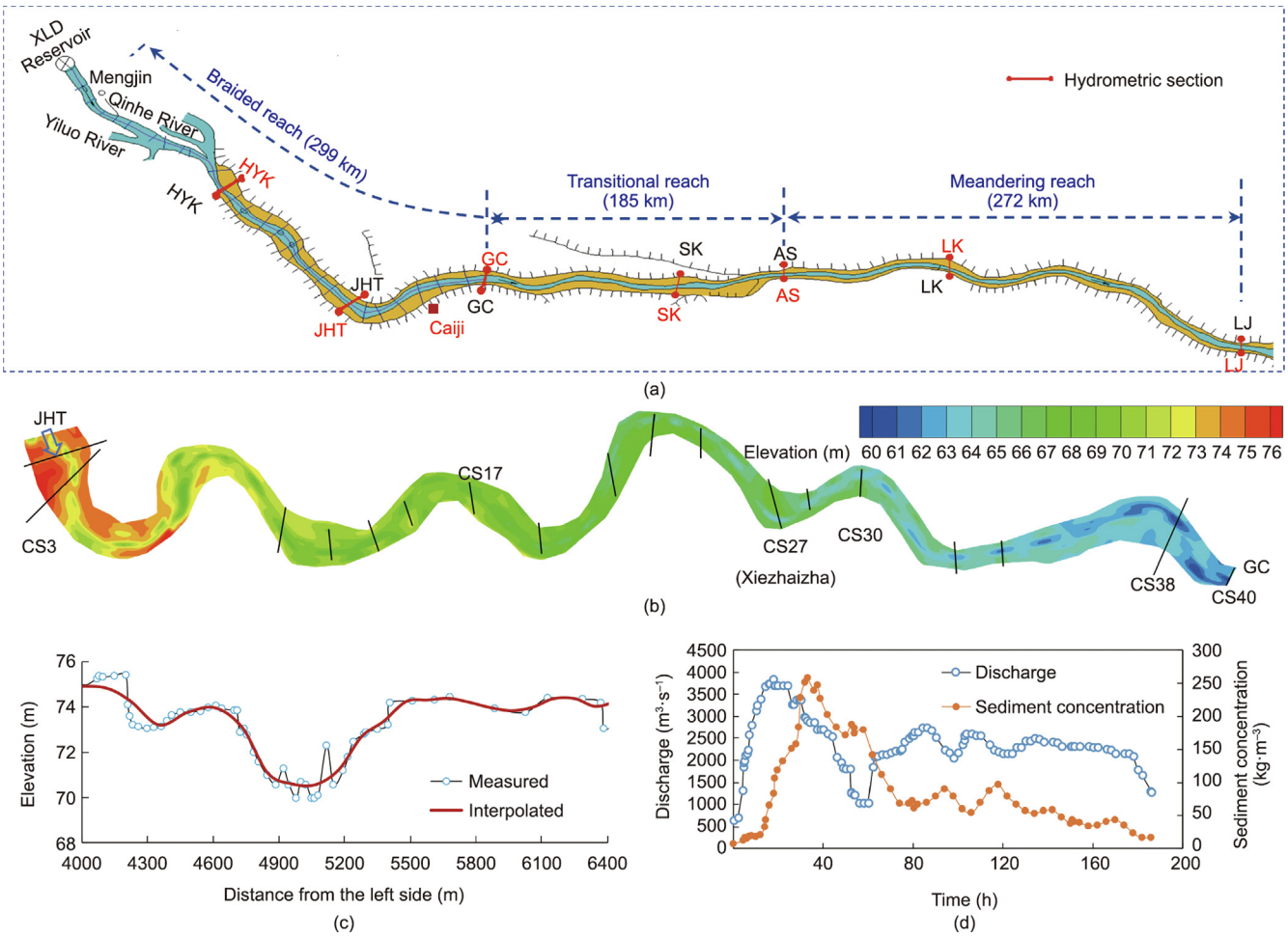

Fig. 4. Overview of the study reach. (a) sketch of the LYR; (b) bed topography of the sub-reach between JHT and GC in 2004; (c) measured and interpolated cross-sectional (CS) profiles at CS3; (d) hydrographs of discharge and sediment concentration at JHT and GC stations. CS: cross-sectional. XLD: Xiaolangdi.

hydrological data, including hydrographs of water level, discharge, sediment concentration, and gradation. These two types of data are provided by the Yellow River Conservancy Commission (YRCC) of the Ministry of Water Resources. The third type includes land use and sensing images. Land use classification was performed using 30 m resolution land use maps and CAD maps, with the latter providing higher accuracy for town location identification. The land use maps were sourced from the Star Cloud Data Service Platform (Pengcheng Laboratory, China), as well as Yang and Huang [42]. The original remote sensing images are downloaded from Geospatial Data Cloud, which is constructed and maintained by the Computer Network Information Center of the Chinese Academy of Sciences.

Based on these data, the accuracy of the integrated model was validated in this section. The 2004 hyperconcentrated flood inundated the main channel zone of the reach between JHT and GC. Therefore, this flood event was simulated to verify the accuracy of the module of 2D morphodynamic processes. A severe dike-breach flood event occurred in 2003 in the Lankao–Dongming (LKDM) floodplain in Henan Province (also located in the reach between JHT and GC), which caused substantial humanitarian and economic losses. Therefore, this dike-breach flood event in the floodplain was simulated to verify the accuracy of the integrated model.

3.1. Modelling of the 2004 hyperconcentrated flood event

3.1.1. Model setup

The LYR refers to the reach extending from Mengjin in Henan Province to LJ in Shandong Province, spanning a total length of 756 km. This reach can be further divided into three distinct regions: the braided, transitional, and meandering reaches (Fig. 4(a)). The reach upstream of GC is defined as the braided reach, which is characterized by multiple channels and central bars. Three hydrometric stations are located in the braided reach to conduct daily hydrological measurements, covering HYK, JHT, and GC. The secondary perched river commonly exists in the sub-reach between JHT and GC with a length of 77 km, where the main flow changes its direction from west to northeast. This reach is densely populated with some large floodplains where the local economy is also growing. Therefore, the sub-reach between JHT and GC was selected as the study reach to verify the 2D morphodynamic module. The cross-sectional topographic data at 40 sedimentation sections in July 2004 were collected to generate the digital terrain (Fig. 4(b)). The cross-sectional profiles are labeled from CS1 to CS40 for easy reference. The interpolated cross-sectional profile at CS3 is plotted to illustrate the accuracy of the generated digital terrain (Fig. 4(c)). The computational domain covered 40 230 meshes, with the mesh area ranging in 717–5831 m^2.

Observed data indicate that the LYR experienced a hyperconcentrated flood event over a short period of approximately one week, from 24 to 31 August 2004 (lasting 186 h). Therefore, the upstream and downstream boundaries were specified as the time series of discharge, sediment concentration, and water level at the JHT and GC stations (Fig. 4(d)). The particle sizes of both suspended load and bed material ranged from 0.002 to 1 mm, and the sediment mixture was divided into nine size fractions to represent its non-uniform characteristics. The value of minimum water depth was set to 0.01 m for treating the evolution of wetting and drying fronts. A constant Manning's roughness coefficient was used in the calibration of the proposed model, and it was found that best results would be provided by a Manning's roughness coefficient of 0.015 for the main channel zone. The time step was set to 0.5 s and the run time under parallel mode was 22.9 h, which was much smaller than that under serial mode (88.8 h).

3.1.2. Simulation results

Comparisons are presented in Fig. 5 between the calculated and measured hydrographs of water level at JHT, as well as discharge and sediment concentration at GC. The calculated water level at JHT rapidly increased to 76.2 m in the first 20 h, which was very close to the measured peak value of 76.3 m. The calculated water level hydrograph also reflected the subsequent declining trend. While the next rising process was overestimated with the calculated second peak value of 76.1 m, which resulted in a low Nash–Sutcliffe efficiency coefficient (NSE) of 0.44 and a root mean square error (RMSE) of 0.22 m. The deviation between the simulated and measured water levels may result from the determination of roughness coefficient. The roughness coefficient was initially set as a constant, and was later modified according to an empirical formula related to water depth. General agreement existed in the calculated and measured discharges at GC, with the RMSE of 430 $m^3 \cdot s^{-1}$. The calculated peak discharge was 4005 $m^3 \cdot s^{-1}$, which was slightly overestimated by 4% compared with the measured peak value of 3840 $m^3 \cdot s^{-1}$. Satisfactory accuracy existed in the simulation of sediment concentration at GC. The model-predicted results using the uncoupled approach are also shown in Fig. 5. A great improvement existed in the simulation of sediment concentration using the coupled approach. The maximum sediment concentration was 180 $kg \cdot m^{-3}$ calculated by the coupled approach and 165 $kg \cdot m^{-3}$ by the uncoupled approach, while the measured maximum was 199 $kg \cdot m^{-3}$. The maximum sediment concentration calculated by the coupled approach was merely underestimated by 9%. The NSE of simulated sediment concentration was 0.73 using the coupled approach and was 0.68 using the uncoupled approach. The corresponding values of RMSE were 27.5 and 30.0 $kg \cdot m^{-3}$, respectively. The results indicate that the 2D morphodynamic module with the coupled approach was efficient to simulate the sediment transport during a hyperconcentrated flood event.

In order to investigate the variation in sediment composition, three groups of sediment are usually classified in the LYR. The grain with the diameter (d) finer than 0.025 mm or greater than 0.050 mm is classified as fine or coarse fraction in the LYR, and the grain with 0.025 mm < $d \leq$ 0.050 mm is classified as the medium one [43]. Fig. 6 shows the comparisons between the calculated and measured graded sediment concentrations at GC in order to further verify the accuracy of the model. The concentration of fine fraction was the largest and there was no coarse fraction at GC. The first calculated maximum concentration of fine fraction was 146 $kg \cdot m^{-3}$, which was very close to the measured value of 144 $kg \cdot m^{-3}$, although the predicted peak concentration slightly lagged behind the measured value (Fig. 6(a)). The calculated hydrograph of medium fraction followed the measured one, but the values were underestimated (Fig. 6(b)). In general, the calculated hydrographs of graded suspended sediment concentration agreed well with the measurements.

3.2. Modelling of the farm-dike breach induced flood event in 2003

3.2.1. Model setup

The LKDM floodplain affected by the 2003 dike-breach flood was located in the "second perched river" between JHT and GC (Fig. 4(a)). Heavy deposition occurred in this reach before the operation of the Xiaolangdi (XLD) Reservoir, which resulted in a low flood discharge capacity with the values of bankfull discharge less than 3000 $m^3 \cdot s^{-1}$ at most sections. Two farm dikes were broken around the flow guide work (FGW) at Caiji in Henan Province (Fig. 4(a)) on 18 September 2003 (Fig. 7(a)), with the variation in cross-sectional profiles near the breach site presented in Fig. 7(b). The main channel greatly migrated towards the right side after two dikes broke during the 2003 flood season, which significantly adjusted the local river regime. The dike-breach width increased to 58 m in a week from 18 to 25 September, and the inundation depth ranged from 0.5–1.5 m over the affected domain. An attempt was made to seal off the breach on 26 September, but failed. The floodplain was inundated for 58 d, which greatly threatened the safety of local inhabitants. Around 1.1 million people were trapped by the flood and more than 7000 buildings were damaged, with the direct economic loss amounting to 0.7 billion CNY.

Controlled by a series of farm dikes and Yellow River levee, the calculation domain was limited to the LKDM floodplain. According to the land use type map and bathymetry map, cropland and towns were extensively distributed over the study area, with an extremely small area of forest (Fig. 7(c)). There was no measured bathymetry of the floodplain in 2003, and therefore the bathymetry measured in 1999 was collected to generate the initial topography (Fig. 7(d)). The computational domain was composed of 27 692

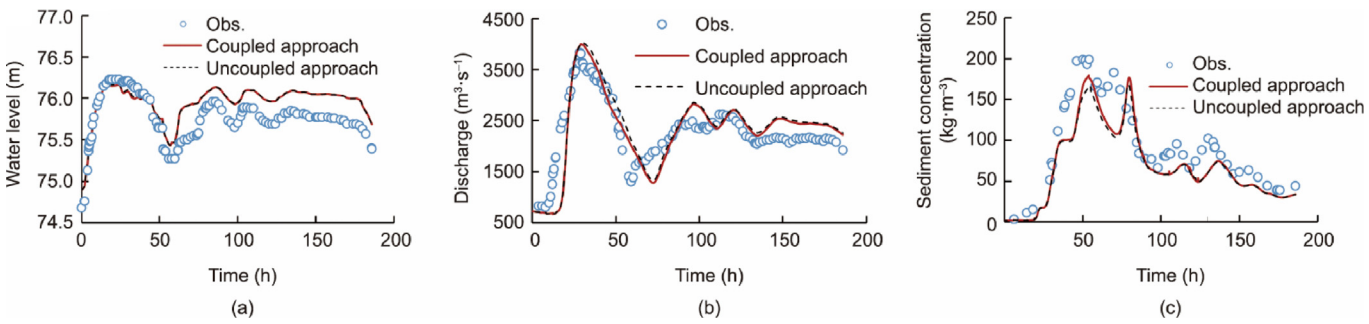

Fig. 5. Comparisons between the simulated and measured hydrographs at different hydrometric stations during the 2004 flood event. (a) Water level at JHT; (b) discharge at GC; (c) sediment concentration at GC. Obs.: observation.

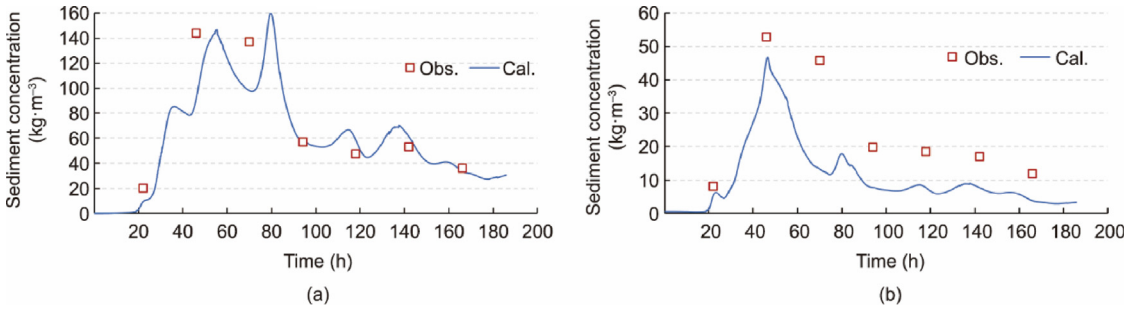

Fig. 6. Comparisons between the simulated and measured hydrographs of graded sediment concentration at GC. (a) Fine fraction with $d \leq 0.025$ mm; (b) medium fraction with 0.025 mm < $d \leq 0.05$ mm. Cal.: calculated value.

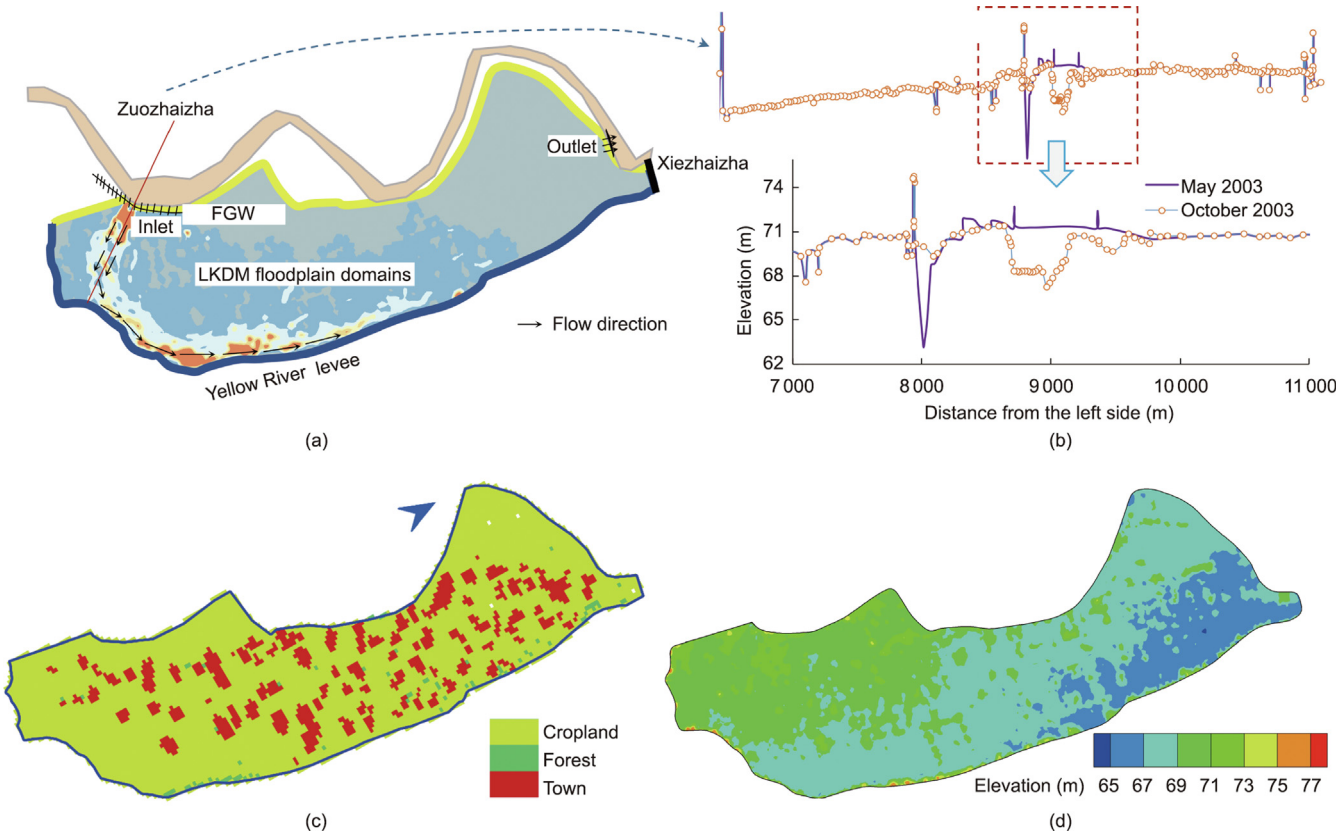

Fig. 7. Description of the dike-breach flood event in 2003. (a) Dike-breach flood inundation processes in the LKDM floodplain. (b) The variation in cross-sectional profiles during a flood season at the breach site of Zuozhaizha; (c) 30 m precision land use type map; (d) topography of the study area.

meshes, with a total area of 199.0 km^2 and the mesh area ranging between 7 and 13 283 m^2. The breach width was set to a constant value of 60 m, with the length of mesh setting to 5 m around the breach site.

There were no measurements related to the flow conditions at the breach site before 3 October 2003. However, the variation in the breach width during the period from 18 to 25 September 2003 was well simulated by Guo et al. [44], and consequently the corresponding simulated discharge hydrograph was adopted as the upstream boundary. The hydrograph of sediment concentration and the gradation of suspended load at JHT during the same period were collected to determine the fractional sediment concentrations at the inlet section.

3.2.2. Simulation results

Fig. 8 illustrates the temporal evolution of the water depth distribution and velocity field after the dike breach. At t = 8 h, the incoming sediment concentration reached a maximum value of 26.9 kg·m^{-3}. The velocity near the breach site shifted downstream (Fig. 8(a)). At t = 80 h, the incoming discharge was small with a value of 100 m^3·s^{-1}, and the flow velocity was 1.5 m·s^{-1} at the breach site. Due to the large transverse slope and lower elevation near the levee, the overbank flow propagated along the levee, with the water depth ranging between 0.8–1.2 m and the velocity smaller than 0.2 m·s^{-1} (Fig. 8(b)). At t = 120 h, the incoming discharge increased to 213 m^3·s^{-1}. The flow rapidly flushed the domain, with the velocity of 2.5 m·s^{-1} at the breach site (Fig. 8(c)). The maximum water depth was around 2.0 m near the levee, and the water depth ranged between 0.4–1.6 m in the inundated floodplain. This simulation results agreed with the record that the inundation depth ranged between 0.5–1.5 m in the LKDM floodplain in five days after the dike breach [45]. At t = 168 h, the incoming discharge reached a maximum value of 439 m^3·s^{-1}. The flow still propagated along the levee, with a maximum depth of 3.4 m (Fig. 8(d)). Most of the floodplain was inundated, with a submerged area of 98 km^2.

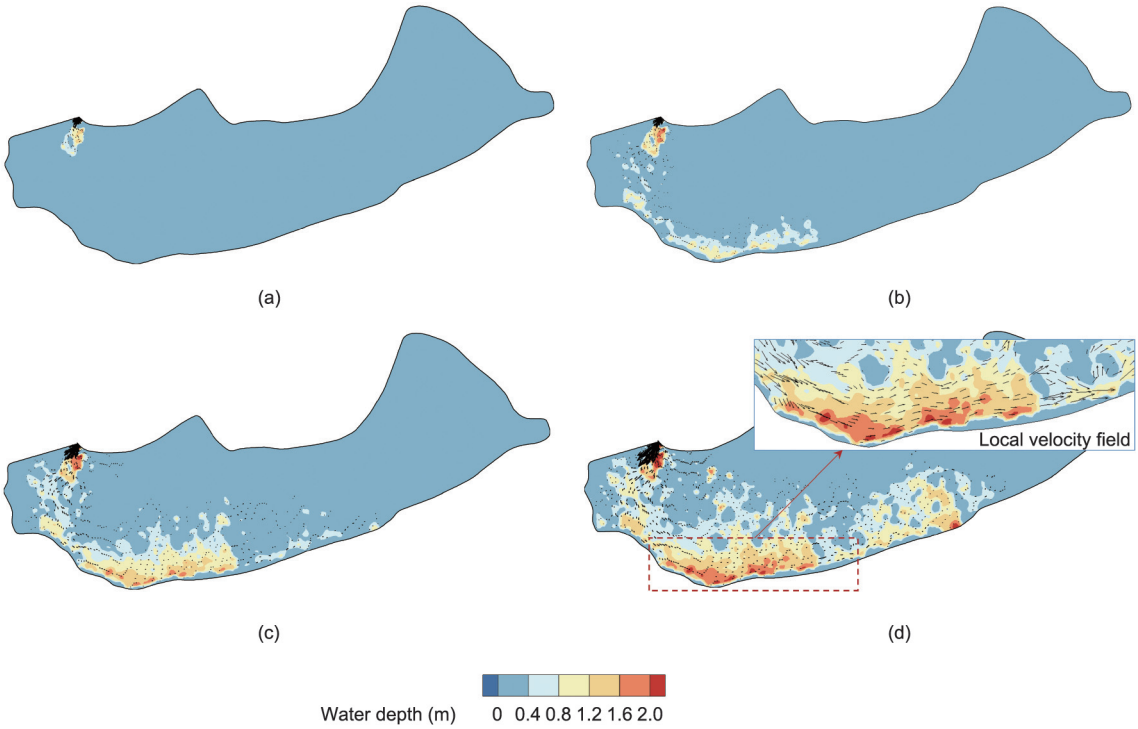

Fig. 8. Simulated water depth distributions and velocity fields at different times of (a) t = 8 h, (b) t = 80 h, (c) t = 120 h, and (d) t = 168 h. The reference flow velocity was set at 1.6 $m \cdot s^{-1}$ for modeling.

The above analyses indicate that the model can simulate the hydrodynamic process of the dike-breach flood over the study domain. Therefore, the evaluation of flood risks to people's life and property was conducted herein. Fig. 9 present the distributions of hazard degree of people and corn at t = 168 h. During the whole simulation period, the hazard degree of people commonly increased to 0.8 along the levee, and people in the central floodplain would be relatively safe with small hazard degrees (Fig. 9(a)). However, the hazard degree and extent of the corn accumulated due to the long inundation duration, with most inundated area facing great losses (Fig. 9(b)).

4. Flood risk evaluation under different floodplain management modes

Different floodplain management modes for the LYR are described in the section, and the vulnerable local reach is identified under an extreme flood with a 1000-year return period through a one-dimensional (1D) morphodynamic model [18]. Then the flood risk evaluation under these management modes has been further conducted using the integrated model. Discussion is mainly concentrated on the inundation extent, duration and hazard degree of each flooded object.

4.1. Different floodplain management modes

The amount of water and sediment is mainly yielded from the upper and middle reaches of the Yellow River basin, but causes severe flood disasters in the LYR [9]. Although the government restricts the local people from living on the floodplains, there is currently no effective way to relocate these residents. The contradiction between the development and flood control of the floodplain highlights exclusive studies on floodplain management modes of the LYR. Currently, three floodplain management schemes are widely discussed: the original mode (referred to as Scheme I for short in this study), the construction of protection embankment mode (Scheme II), and the floodplain partition harnessing mode (Scheme III).

The key of the mode of Scheme II is to construct consecutive protection embankment, in order to shape a stable and wide main

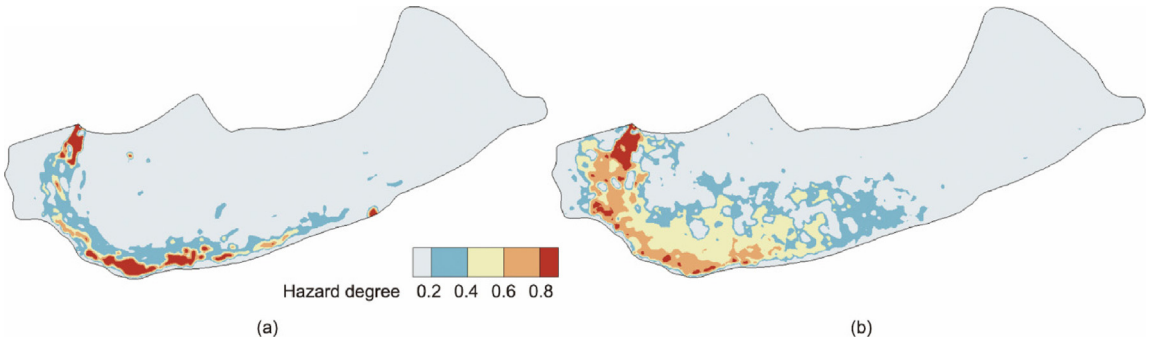

Fig. 9. Simulated distributions of hazard degree at t = 168 h for (a) people and (b) corn.

channel with the channel width varying from 2.0–3.0 km, which can convey the flood with a peak discharge of 10 000 $m^3 \cdot s^{-1}$ [46,47]. The elevation inside and outside the embankment would not be modified. The aim of the Scheme III is to partition the current floodplain into different zones by increasing the elevation of local floodplain [3]. The specific plan for each partitioned zone includes: ① The floodplain 2 000 m away from the levee will be modified as a high floodplain, which can thereby accommodate residents and withstand the flood with a 20-year return period (the corresponding peak discharge is around 10 000 $m^3 \cdot s^{-1}$ at JHT); ② the low floodplain zone will be classified by the existing FGWs and connection dikes, and it can withstand the flood with a 5-year return period (the corresponding peak discharge is 8 000 $m^3 \cdot s^{-1}$ at JHT), which can be further utilized for ecological and sightseeing agriculture; and ③ the marginal floodplain adjacent to the current main channel will be treated as ecological wetlands without any human activities, which will also convey the flow and sediment during flood seasons. The cross-sectional profiles after modification of the three schemes are presented in Fig. 10.

4.2. Quantification of the vulnerable local reach under an extreme flood

The flood event occurring in July of 1958 was the largest flood in record in the LYR, with a peak discharge of 16 700 $m^3 \cdot s^{-1}$ at the XLD station, and 22 300 $m^3 \cdot s^{-1}$ at the HYK station. It is estimated that the flood event had a return period of 1000 years in the LYR [18,48]. Therefore, the extreme flood event is regarded as the most unfavorable flow regime of the LYR. The regulation effects of the powerful XLD Reservoir should be put into consideration when simulating the extreme flood under the current topography in 2020. The 1D morphodynamic model for reservoirs and rivers proposed by Xia et al. [18] was adopted to calculate the flow and sediment transport processes in the reservoir and the LYR. The flow and sediment condition entering the XLD Reservoir during the period from July 11 to 24, 1958 (lasting 316 h) was adopted as the upstream boundary conditions, and the cross-sectional profiles and bed material composition prior to the 2020 flood season were collected as the current channel boundary conditions. The simulated hydrographs of discharge and sediment concentration at different sections are presented in Figs. 11(a) and (b). In 2020, the minimum bankfull discharge was 4 375 $m^3 \cdot s^{-1}$ and the maximum bankfull discharge was less than 10 000 $m^3 \cdot s^{-1}$ in the LYR. The reach-scale bankfull discharge was 8 713 $m^3 \cdot s^{-1}$ in the braided reach, 6 155 $m^3 \cdot s^{-1}$ in the transitional reach, and 6 384 $m^3 \cdot s^{-1}$ in the meandering reach. As a consequence, a phenomenon of overbank flow would occur along the LYR. The duration and magnitude (represented by the ratio of maximum discharge to bankfull discharge) of the overbank flow were calculated at each section along the LYR, as shown in Fig. 11(c). It can be concluded that the 77 km long reach between JHT and GC would be the most vulnerable, with the average duration and magnitude of overbank flow being equal to 140 h and 1.4 respectively.

The river width of the fluvial region encompassed between the left and right levees ranges in 5.0–20.0 km in the reach between JHT and GC, and the width of floodplains accounts for around 70% of the whole cross-sectional width. Two large floodplains are densely populated in the reach, covering the Changyuan (CY) and the LKDM floodplains in Henan Province. The computation domain covered 58 133 meshes, with the total area of 748.0 km^2 (including the floodplain area of 640.7 km^2) and the area of each cell ranging between 455 m^2 and 0.05 km^2. The topography of the main channel in the study reach was generated based on the cross-sectional

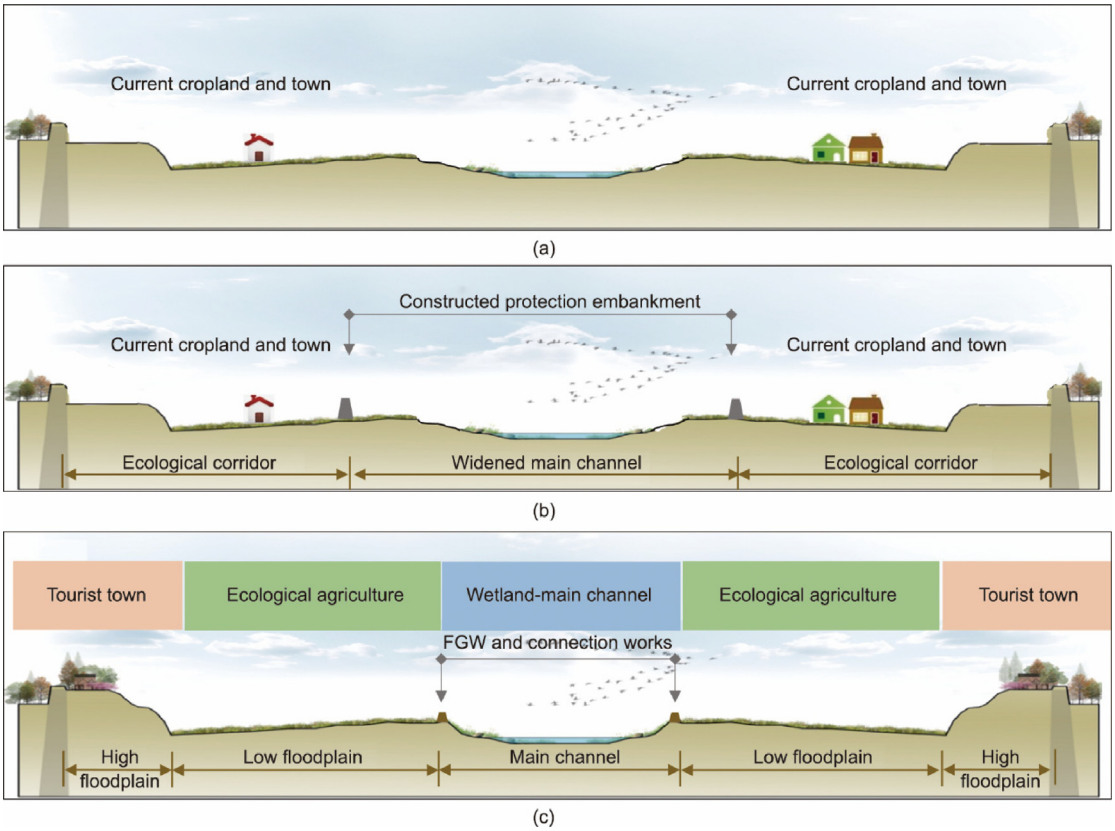

Fig. 10. Cross-sectional profiles after modifications of different floodplain management modes. (a) Scheme I; (b) Scheme II; (c) Scheme III.

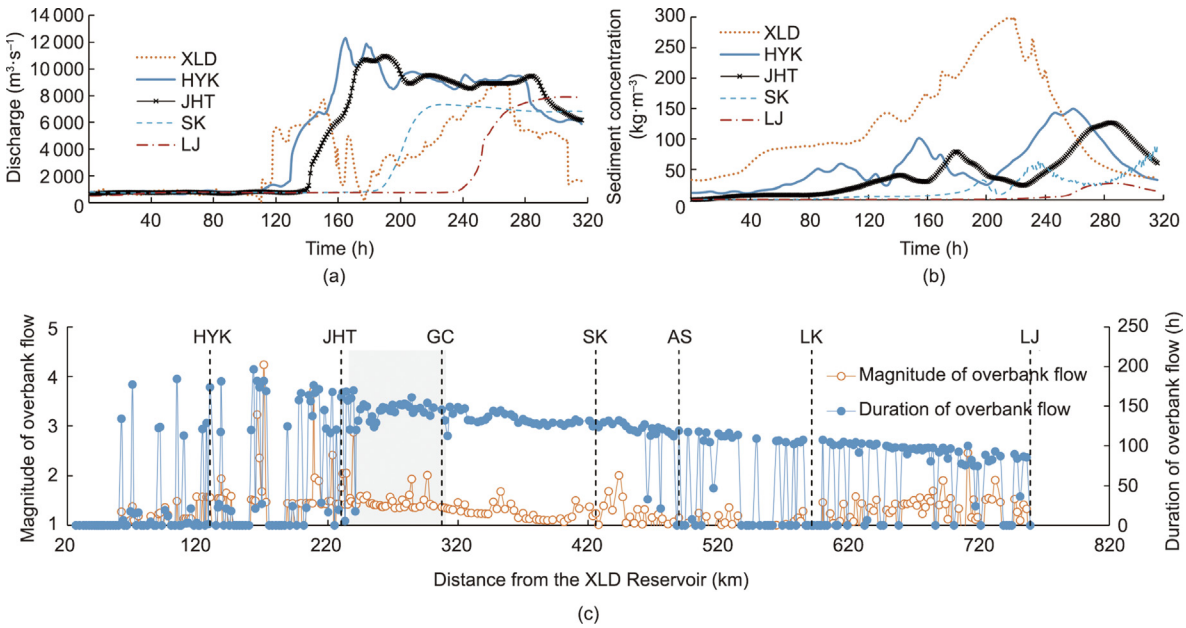

Fig. 11. Characteristics of the extreme flood routing process: simulated hydrographs of (a) discharge and (b) sediment concentration; and (c) duration and magnitude of the overbank flow along the LYR under the topography in 2020.

profiles at 40 sedimentation sections before the 2020 flood season, and the topography of the floodplains was generated by the bathymetry measured in 2012 due to the lack of recent measurements (Fig. 12(a)). The land use types of the floodplains included bare land, cropland, forest, town, and river regulation works, which were labelled using different point codes (Cod = 1–5) at the computational nodes. Specifically, a node belonging to the bare land is marked as Cod = 1, and a node implemented with the regulation works is marked as Cod = 5. The corresponding roughness coefficient was set to vary between 0.020 and 0.065 for different point codes on the floodplains, and the roughness coefficient of main channel was set to a constant value of 0.018. The specific zoning of the computational domain under different floodplain management schemes is also presented in Figs. 12(a) and (b). The levels of protection embankment and high/low floodplain were determined based on the relationship between water level and discharge at each section. Therefore, the elevation of protection embankment in the Scheme II and the high floodplain in the Scheme III would vary from 63.7 to 74.3 m corresponding to the discharge of 10 000 $m^3 \cdot s^{-1}$. Due to the relatively large area of low floodplain, only the elevation of corresponding division line would be heightened to 62.8 to 73.7 m corresponding to the discharge of 8 000 $m^3 \cdot s^{-1}$ in the Scheme . Due to the difficulty in the prediction of breach site, the breach of river regulation works was not considered in the current study.

4.3. Flood risk evaluation under different management modes

4.3.1. Inundation extent

Identifying the inundation extent is critical to flood risk mitigation. The inundation areas at the maximum inundation depth were calculated under different floodplain management modes. The maximum inundation depth (h_m) was the maximum water depth in a cell during the whole simulation period, which could reflect the highest flood risk to some extent. According to the values of inundation depth, three classes of inundation degree were determined [49]: slight inundation degree with h_m less than 0.5 m, medium inundation degree with h_m varying from 0.5 to 1.5 m, and heavy inundation degree with h_m larger than 1.5 m. The graded inundation extents are shown in Table 1. Without any modification (Scheme I), the current study domain was predicted to be extensively inundated, with most of the floodplains (around 547.8 km^2) in medium and heavy inundation degrees. Even worse, approximately 262.6 km^2 would experience a heavy inundation degree, which represented around 41% of the total floodplains. Under Scheme II, the situation would be changed, with the area

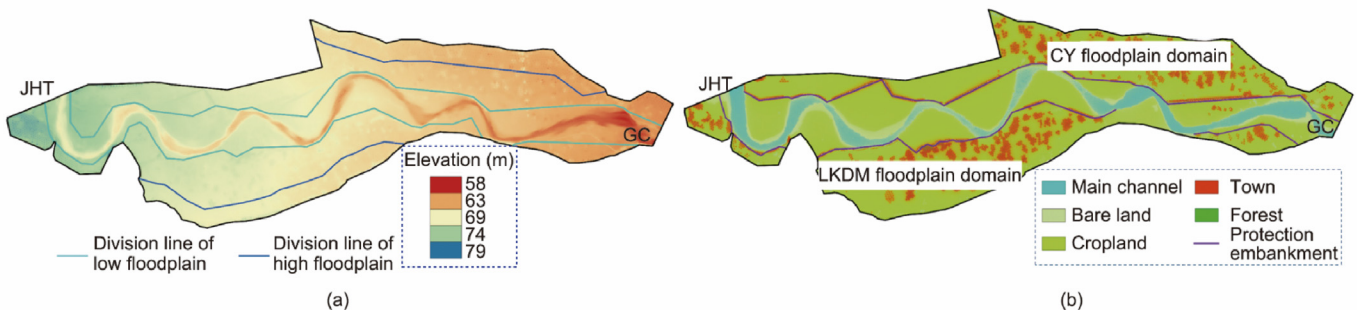

Fig. 12. Topography, land use types, and specific zoning of different schemes imposed on the computational domain. (a) Bed topography in 2020 and the zoning of the Scheme III; (b) land use types and the zoning of the Scheme II.

Table 1
Areas and ratios of the floodplains for various inundation degrees under different management modes.

Management mode	Slight inundation degree		Medium inundation degree		Heavy inundation degree	
	Area (km^2)	Ratio (%)	Area (km^2)	Ratio (%)	Area (km^2)	Ratio (%)
Scheme I	92.9	14.5	285.2	44.5	262.6	41.0
Scheme II	283.6	44.3	206.3	32.2	150.8	23.5
Scheme III	96.4	15.1	391.2	61.1	153.1	23.9

in slight and medium inundation degrees dominating. Around 44% of the total floodplains would be in slight inundation degree, but there would be still some domains in heavy inundation degree of around 150.8 km^2. Under Scheme III, the area in medium inundation degree would dominate, which would account for around 61% of the total floodplains. It can be concluded from Table 1 and Figs. 13(a)–(c) that most of the floodplains would be in heavy inundation degree in the current topography under the extreme flood event. Due to the improved flood discharge capacity along the reach under Scheme II, the inundation extent would be alleviated, with most domains in slight inundation degree. The flood control standard would be merely improved on the high floodplain under Scheme III, and therefore most domains would be in medium inundation degree.

4.3.2. Inundation duration

Inundation duration is one of the important indicators in flood risk assessment, which is especially critical to the hazard degree for crops. As stated before, corn will get affected when the water depth exceeds 0.1 m (Fig. 3(b)). Therefore, two characteristic water depths including the minimum water depth during simulation (0.01 m) and the minimum water depth to affect the growth of corn (0.1 m), were adopted to calculate the inundation duration of the whole floodplains. According to the standard classes for flood inundation duration [49], four classes were determined in the current study: T_{in} less than 24 h (I-class), T_{in} in the range of 1–3 d (II-class), T_{in} in the range of 3–7 d (III-class), and T_{in} larger than 7 d (IV-class). The graded inundation duration is presented in Table 2.

It can be found that there was a slight variation in inundation duration when different characteristic water depths were used. Taking the results in Table 2 as an example (the characteristic water depth was 0.01 m), it can be concluded that: ① Extremely small domains would be inundated for II-class, while most domains would be inundated for III-class. The whole simulation period was 316 h, which indicated that most domains would be in long-term inundation under this extreme flood event. ② Under Scheme II, approximately 20% of the entire study area would be inundated by floods of I-class. Among this 20% of the inundated area, about 10% of the entire study area would be inundated by floods of III-class under Scheme I. The area inundated by floods of IV-class under Scheme II accounts for 6.1%, which is slightly larger than the 5.0% of the area inundated by floods of IV-class under Scheme I. This difference is due to the fact that the protection embankments in Scheme II hinder the exchange of water and sediment. ③ Under Scheme III, extremely small domains would be inundated for IV-class compared with other schemes, which indicated that the process of flood recession would be rapid due to the free exchange of water and sediment between the main channel and floodplains. In addition, around 20% of the high floodplains (26.0 km^2) would be inundated for I-class, and no high floodplain was predicted to be inundated for IV-class.

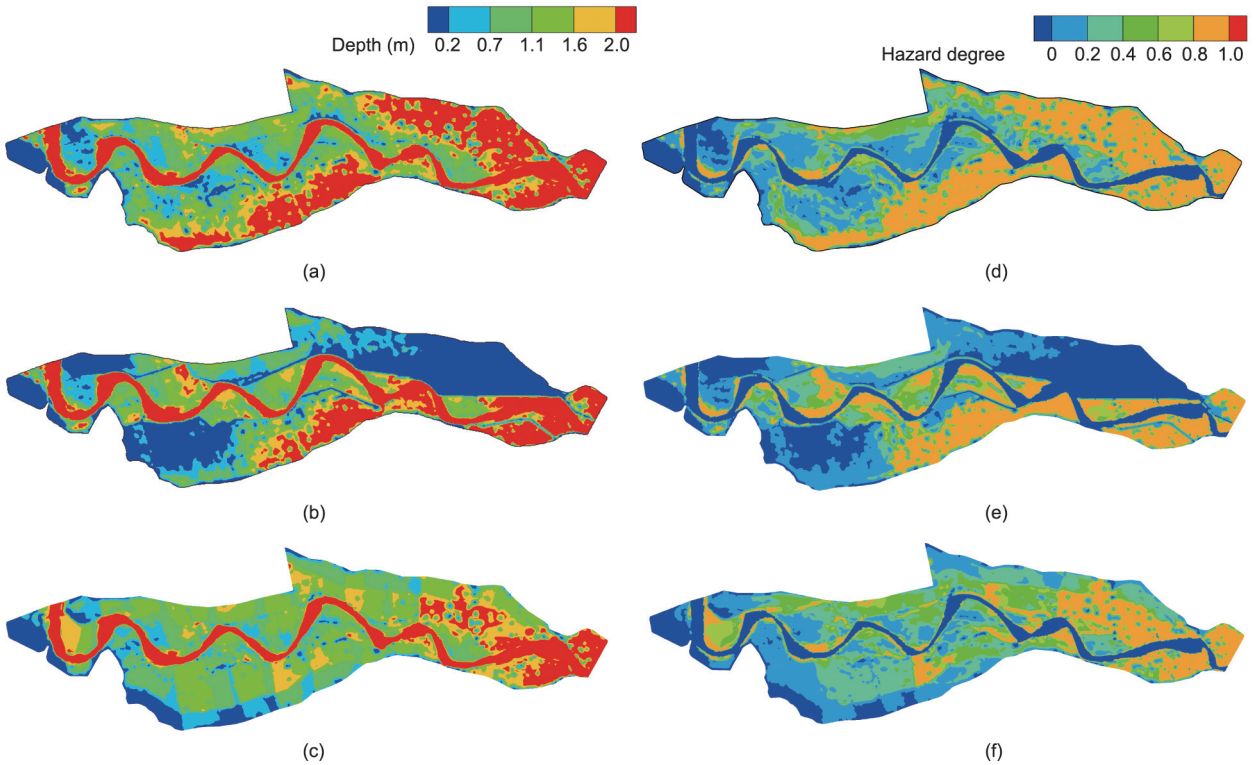

Fig. 13. Predicted inundation extents under (a) Scheme I, (b) Scheme II, and (c) Scheme III; predicted maximum hazard degrees of people under (d) Scheme I, (e) Scheme II, and (f) Scheme III.

Table 2
Corresponding area and ratio of each graded inundation duration under different floodplain management modes.

Characteristic water depth (m)	Management modes	I-class		II-class		III-class		IV-class	
		Area (km^2)	Ratio (%)	Area (km^2)	Ratio (%)	Area (km^2)	Ratio (%)	Area (km^2)	Ratio (%)
0.01	Scheme I	51.2	8.0	10.1	1.6	547.1	85.4	32.3	5.0
	Scheme II	122.4	19.1	23.9	3.7	455.3	71.1	39.2	6.1
	Scheme III	44.8	7.0	6.7	1.1	587.2	91.6	2.0	0.3
0.1	Scheme I	62.0	9.7	15.5	2.4	559.4	87.3	3.8	0.6
	Scheme II	137.7	21.5	29.5	4.6	465.3	72.6	8.2	1.3
	Scheme III	55.8	8.7	10.0	1.6	573.1	89.5	1.8	0.3

Graded inundation duration [49]: I-class with T_{in} (0, 24 h), II-class with T_{in} (24, 72 h), III-class with T_{in} (72, 168 h), IV-class with T_{in} (168 h, $+\infty$)

4.3.3. Flood hazard degree of each flooded object

This section highlights the effects of different floodplain management modes on the flood hazard degree of each flooded object. Figs. 13(d)–(f) show the spatial distributions of simulated maximum hazard degrees of people in the affected areas. It is suggested that people would face a higher flood risk under Scheme I, with the hazard degree larger than 0.80 over most domains. The inhabitants in the domains inside the protection embankments would suffer from a high flood risk under Scheme II. Owing to the Scheme II, the inhabitants in the CY floodplain on the left side would be relatively safe. However, the inhabitants in the LKDM floodplain on the right side would still face a great threat, with the maximum hazard degree exceeding 0.8. Under Scheme III, the inhabitants in the high floodplains would be safe, with the maximum hazard degree lower than 0.2, while a great threat would exist in some low floodplains. In addition, the domains near the outlet would be very dangerous under all the management modes, necessitating restrictions on public access.

In order to further illustrate the flood damage to each flooded object, the variations in the area with high risk are presented in Fig. 14 and Table 3. Based on the land use types, the total areas of buildings and cropland were 39.8 and 529.5 km^2, respectively. Considering human activities over the floodplains, the total area with people's presence was 640.7 km^2. Then the ratio of the high-risk area to the corresponding total area for each object was calculated in Table 3. The variation in high-risk area for each flooded object was in consistence with the mechanism of each object being damaged. The hazard degrees of people and buildings were closely related to the variation in water depth and flow velocity, and therefore the high-risk area would reduce during the flood recession. The hazard degree for corn was directly proportional to inundation duration, which resulted in a continuous increase in the high-risk area for corn (Fig. 14). It can be concluded from Table 3 that: ① The high-risk area would be the maximum under Scheme I for each object, with the inhabitants in half of the domains facing a high hazard degree. Great damages would be imposed on the crop, with more than 64.0 km^2 area at high risk. ② Under Scheme II, the high-risk area would be the minimum for people. However, there would be a quantity of cropland inside the protection embankments, and therefore around 33.1 km^2 cropland would be at high risk. ③ Under Scheme III, the high-risk area for people would be slightly larger than the value under Scheme II. While the high-risk area for buildings and crop would be the smallest compared with other schemes, which would account for 0.3% of the total town area and 0.8% of the total cropland. The high-risk area for people and buildings on the high floodplains was additionally calculated, which indicated that the inhabitants in the domains of 7.3 km^2 would be at high risk and no buildings would be at high risk. As a consequence, the flood risk to each object would significantly reduce under Scheme III. If strict restrictions are imposed on human activities on low floodplains during large floods, each object will be much safer under Scheme III.

4.3.4. Comprehensive evaluation for people's life and property

It is necessary to consider the socio-economic resilience in the flood risk evaluation, which usually needs detailed socio-economic data such as the distribution of gross domestic product (GDP) and population density. However, the collected maps are not accurate to reflect the distribution of economy and infrastructure in the floodplain domains in the LYR, because almost all buildings are accumulated in the LKDM and CY floodplains and crops are distributed in other domains. Therefore, it is reasonable to calculate the flood risk based on damage curve and the land use types in the study area. The average flood risk ($\bar{R}$) to people's life and property is added to comprehensively evaluate the effect of different floodplain management schemes. Based on the assumption that the weight of each flooded object is equal in the assessment, $\bar{R}$ is calculated by the following expression:

$$\bar{R} = \sum_{l=1}^{3} \bar{R}_l / 3 \tag{8}$$

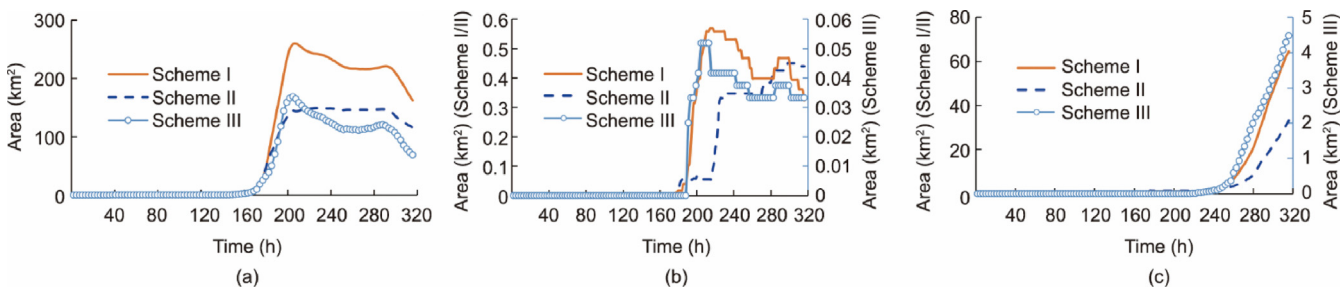

Fig. 14. Temporal variations in the high-risk area for each object under different management modes. (a) People; (b) buildings; (c) crop.

Table 3
Area and ratio of domains at high risk (hazard degree > 0.85) for each object under different management modes.

Management mode	People		Buildings		Crop	
	Area (km^2)	Ratio (%)	Area (km^2)	Ratio (%)	Area (km^2)	Ratio (%)
Scheme I	259.9	40.6	0.6	1.5	64.6	12.2
Scheme II	149.5	23.3	0.5	1.3	33.1	6.3
Scheme III	168.9	26.4	0.1	0.3	4.5	0.8

$$\bar{R}_l = \sum_{i=1}^{N}(\mathrm{HD}_l \times A_i)/\sum_{i=1}^{N} A_i \quad (9)$$

where A_i is the area of the ith mesh with people, buildings, or corn; HD_l is the according maximum hazard degree of people (l = 1), buildings (l = 2), and corn (l = 3) in A_i during a flood event; $\bar{R}_l$ is the average value of maximum hazard degree of people (l = 1), buildings (l = 2), and corn (l = 3) in the study area; and N is the total meshes. Then this indicator not only comprehensively quantifies the flood risk of the study area, but also considers the distribution of people, buildings and crops, which indirectly reflects the socio-economic dimensions in the flood risk assessment.

The calculation results of flood risks under different management modes are represented in Table 4. The average flood risk to people's life and property was 0.52 under Scheme I, 0.32 under Scheme II, and 0.37 under Scheme III. In summary, the average flood risk was significantly reduced and similar under Scheme II and III, but the high-risk area for each flooded object would be significantly reduced under Scheme III.

Finally, some other socio-economic factors should be put into consideration when implementing the floodplain management mode. It should be noted that there was no community displacement when evaluating the flood risk under each floodplain management mode, in order to compare the effects of different schemes. Therefore, the results obtained from the current study can help to determine the dangerous domains and displaced population if detailed data available. However, the relevant departments should further consider the choice of new displacement location and support of infrastructure based on the migrated population, in order to make an optimal plan of community displacement. In addition, it is important but hard to estimate the exact cost of each floodplain management mode, because it involves the embankment construction, artificial deposition and community displacement. Therefore, the current study aims to provide a preliminary evaluation of different floodplain management modes in terms of flood risk, offering insights to estimate the population displacement. The choice of floodplain management mode can be made after the comprehensive consideration of the departments of land planning, water conservancy, finance and other relevant departments based on the evaluation results obtained in the current study.

5. Summary and conclusions

Future increases in flood severity due to climate changes are expected in the LYR, which will have detrimental impacts on human activities and economic development. Therefore, there is an urgent need to conduct the flood risk evaluation in the LYR under different floodplain management modes, in order to support the management and development of the densely populated floodplains. An integrated model was proposed, including the modules of 2D morphodynamicl processes and flood risk evaluation, which is especially developed for the complex bathymetry and high sediment load in the LYR. The proposed model was validated by the hyperconcentrated flood event and the dike-breach induced flood event. Then the model was further applied to evaluate the flood risks to people's life and property of key floodplains under different management modes. The following conclusions can be obtained.

(1) An integrated model was proposed, including a module of 2D morphodynamicl processes and a module of flood risk evaluation. The module of 2D morphodynamic processes directly accounted for the effects of the spatial variations in sediment concentration and bed deformation in the hydrodynamic equations. The module of flood risk evaluation coupled some improved calculation relations of hazard degree for people's life and property, which were derived from mechanical analyses and sufficient field surveys. The flood risk assessment technique was greatly improved, with the flood risks to people's life and property being evaluated based on the predicted hydrodynamic parameters and the adopted hazard degree relations.

(2) Good accuracy of the integrated model was presented in the simulation of two flood events. The calculated graded sediment concentrations were close to the measured hydrographs, and the maximum total sediment concentration was just underestimated by 9%. The simulated inundation depth agreed well with the field record.

(3) Effects of different floodplain management modes were quantified on the human and economic losses under an extreme flood event. Most domains would be inundated for 3–7 d under Scheme II, and extremely small domains would be inundated for more than 7 d under Scheme III. The average flood risk to people's life and property would be the largest under Scheme I, which would be similar under Scheme II and III. But compared with Scheme I, the high-risk area for people's life and property would reduce by 21%–49% under Scheme II, which would reduce by 35%–93% under Scheme III.

Table 4
Average flood risks to people's life and property under different management modes.

Management mode	$\bar{R}_1$	$\bar{R}_2$	$\bar{R}_3$	$\bar{R}$
Scheme I	0.59	0.34	0.63	0.52
Scheme II	0.36	0.36	0.23	0.32
Scheme III	0.52	0.14	0.20	0.37

CRediT authorship contribution statement

Yifei Cheng: Writing – review & editing, Writing – original draft, Software, Methodology, Conceptualization. **Junqiang Xia:** Writing – review & editing, Supervision, Investigation, Funding acquisition. **Hongwei Fang:** Writing – review & editing, Investigation. **Meirong Zhou:** Validation, Investigation. **Zuhao Zhou:** Validation, Supervision. **Jun Lu:** Resources, Data curation. **Dongyang Li:** Resources. **Roger A. Falconer:** Writing – review & editing. **Yuchuan Bai:** Writing – review & editing.

Declaration of competing interest

The authors declare that they have no known competing financial interests or personal relationships that could have appeared to influence the work reported in this paper.

Acknowledgments

The work was supported by the National Natural Science Foundation of China (U2243238) and the Program of the National Key Research and Development Plan (2023YFC3209304).

Appendix A. Supplementary data

Supplementary data to this article can be found online at https://doi.org/10.1016/j.eng.2025.02.011.

References

[1] Leskens J, Brugnach M, Hoekstra AY, Schuurmans W. Why are decisions in flood disaster management so poorly supported by information from flood models? Environ Model Softw 2014;53:53–61.
[2] Parvin GA, Shimi AC, Shaw R, Biswas C. Flood in a changing climate: the impact on livelihood and how the rural poor cope in Bangladesh. Climate 2016;4(4):60.
[3] Zhang JL, Shang YZ, Cui M, Luo Q, Zhang R. Successful and sustainable governance of the lower Yellow River, China: a floodplain utilization approach for balancing ecological conservation and development. Environ Dev Sustain 2022;24(3):3014–38.
[4] Winsemius HC, Aerts JCJH, van Beek LPH, Bierkens MFP, Bouwman A, Jongman B, et al. Global drivers of future river flood risk. Nat Clim Chang 2016;6(4):381–5.
[5] Dottori F, Szewczyk W, Ciscar JC, Zhao F, Alfieri L, Hirabayashi Y, et al. Increased human and economic losses from river flooding with anthropogenic warming. Nat Clim Chang 2018;8(9):781–6.
[6] Intergovernmental Panel on Climate Change (IPCC). Managing the risks of extreme events and disasters to advance climate change adaptation. Cambridge: Cambridge University Press; 2012.
[7] Jongman B, Ward PJ, Aerts JCJH. Global exposure to river and coastal flooding: long term trends and changes. Glob Environ Change 2012;22(4):823–35.
[8] Visser H, Petersen AC, Ligtvoet W. On the relation between weather-related disaster impacts, vulnerability and climate change. Clim Change 2014;125(3–4):461–77.
[9] Wang H, Zhao Y. Preliminary study on harnessing strategies for Yellow River in the new period. J Hydraul Eng 2019;50(11):1291–8. Chinese.
[10] Hamilton SK, Sippel SJ, Melack JM. Comparison of inundation patterns among major South American floodplains. J Geophys Res D Atmospheres 2002;107(D20):8038.
[11] Bates PD. Flood inundation prediction. Annu Rev Fluid Mech 2022;54(1):287–315.
[12] Manavalan R. SAR image analysis techniques for flood area mapping-literature survey. Earth Sci Inform 2017;10(1):1–14.
[13] Clement MA, Kilsby CG, Moore P. Multi-temporal synthetic aperture radar flood mapping using change detection. J Flood Risk Manag 2018;11(2):152–68.
[14] Melkamu T, Bagyaraj M, Adimaw M, Ngusie A, Karuppannan S. Detecting and mapping flood inundation areas in Fogera–Dera Floodplain, Ethiopia during an extreme wet season using Sentinel–1 data. Phys Chem Earth 2022;127:103189.
[15] Sleigh PA, Gaskell PH, Berzins M, Wright NG. An unstructured finite-volume algorithm for predicting flow in rivers and estuaries. Comput Fluids 1998;27(4):479–508.
[16] Caleffi V, Valiani A, Zanni A. Finite volume method for simulating extreme flood events in natural channels. J Hydraul Res 2003;41(2):167–77.
[17] Yoon TH, Kang SK. Finite volume model for two-dimensional shallow water flows on unstructured grids. J Hydraul Eng 2004;130(7):678–88. Chinese.
[18] Xia JQ, Wang ZH, Wang YZ, Zhang XL. Development and application of a reservoir–channel–floodplain coupling model system for flow and sediment transport in the middle and lower Yellow River. J Basic Sci Eng 2020;28(6):652–65. Chinese.
[19] Hou JM, Kang YD, Hu CH, Tong Y, Pan B, Xia J. A GPU-based numerical model coupling hydrodynamical and morphological processes. Int J Sediment Res 2020;35(4):386–94.
[20] Yue ZY, Liu QQ, Huang W, Hu P, Cao Z. 2D well-balanced, coupled model of water flow, sediment transport, and bed evolution based on unstructured grids with efficient variable storage strategy. Int J Sediment Res 2021;36(1):151–60.
[21] Zapata Uh, Gamboa Salazar L, Itzá Balam R, Nguyen KD. An unstructured finite-volume semi-coupled projection model for bed load sediment transport in shallow-water flows. J Hydraul Res 2021;59(4):545–58.
[22] Xia JQ, Lin BL, Falconer RA, Wang G. Modelling dam-break flows over mobile beds using a 2D coupled approach. Adv Water Resour 2010;33(2):171–83.
[23] Martínez-Aranda S, Murillo J, García-Navarro P. Comparison of new efficient 2D models for the simulation of bedload transport using the augmented Roe approach. Adv Water Resour 2021;153:103931.
[24] Wallingford HR. R&D outputs: flood risks to people (Phase 2). London: Defra and Environment Agency (EA); 2006.
[25] Xia JQ, Falconer RA, Wang YJ, Xiao X. New criterion for the stability of a human body in floodwaters. J Hydraul Res 2014;52(1):93–104.
[26] Kvočka D, Falconer RA, Bray M. Flood hazard assessment for extreme flood events. Nat Hazards 2016;84(3):1569–99.
[27] Wang N, Hou JM, Du YG, Jing H, Wang T, Xia J, et al. A dynamic, convenient and accurate method for assessing the flood risk of people and vehicle. Sci Total Environ 2021;797:149036.
[28] Dong BL, Xia JQ, Zhou MR, Li Q, Ahmadian R, Falconer RA. Integrated modeling of 2D urban surface and 1D sewer hydrodynamic processes and flood risk assessment of people and vehicles. Sci Total Environ 2022;827:154098.
[29] Krzysztofowicz R, Davis DR. Category-unit loss functions for flood forecast–response system evaluation. Water Resour Res 1983;19(6):1476–80.
[30] Dutta D, Herath S, Musiake K. A mathematical model for flood loss estimation. J Hydrol 2003;277(1–2):24–49.
[31] Simpson G, Castelltort S. Coupled model of surface water flow, sediment transport and morphological evolution. Comput Geosci 2006;32(10):1600–14.
[32] Milanesi L, Pilotti M, Ranzi R. A conceptual model of people's vulnerability to floods. Water Resour Res 2015;51(1):182–97.
[33] Chanson H, Brown R. New criterion for the stability of a human body in floodwaters. J Hydraul Res 2015;53(4):540–1.
[34] Parker DJ, Green CH, Thompson PM. Urban flood protection benefits: a project appraisal guide. London: Gower Technical Press; 1987.
[35] Suleman MS, N'Jai A, Green CH, Penning-Rowsell EC. Potential flood damage data: a major update. London: Middlesex Polytechnic Flood Hazard Research Centre; 1988.
[36] Smith DI. Flood damage estimation—a review of urban stage-damage curves and loss functions. Water SA 1994;20(3):231–8.
[37] Kelman H. Physical flood vulnerability of residential properties in coastal, eastern England [dissertation]. Cambridge: University of Cambridge; 2002.
[38] Guo P, Xia JQ, Zhou MR, Falconer RA, Wang Z, Chen Q. Modelling of flood risks to people and property in a flood diversion zone. J Zhejiang Univ Sci A 2018;19(11):864–77.
[39] Klaus S, Kreibich H, Merz B, Kuhlmann B, Schröter K. Large-scale, seasonal flood risk analysis for agricultural crops in Germany. Environ Earth Sci 2016;75(18):1289.
[40] Pacetti T, Caporali E, Rulli MC. Floods and food security: a method to estimate the effect of inundation on crops availability. Adv Water Resour 2017;110:494–504.
[41] Xia JQ, Falconer RA, Lin BL, Tan G. Numerical assessment of flood hazard risk to people and vehicles in flash floods. Environ Model Softw 2011;26(8):987–98.
[42] Yang J, Huang X. The 30 m annual land cover dataset and its dynamics in China from 1990 to 2019. Earth Syst Sci Data 2021;13(8):3907–25.
[43] Long YQ, Chien N. Erosion and transportation of sediment in the Yellow River basin. Int J Sediment Res 1986;1(1):2–38.
[44] Guo P, Xia JQ, Zhou MR. Numerical modelling of farm dike lateral breach induced by flooding processes. Sediment Res 2022;47(6):15–22. Chinese.
[45] Yellow River Conservancy Commission of the Ministry of Water Resources. Revelation of flood rescue at Caiji in the lower Yellow River. Zhengzhou: Yellow River Press; 2008. Chinese.
[46] Li WX, Li Y. Integration of the Yellow River harnessing strategies of "keeping a broad flood plain with solid embankment" and "clearing sediments by means of converting flow." J Hydraul Eng 2002;10:96–102. Chinese.
[47] Tian Y, Qu B, Li Y, Gu ZG. Research and perspective on floodplain treatment in the lower Yellow River. Yellow River 2019;41(2):14–9. Chinese.
[48] Chen ZT, Hu RN, Zhang YL. Introduction to the Yellow River flood in July 1958. Hydrology 1981;3:44–7. Chinese.
[49] Ministry of Water Resources of the People's Republic of China. Guidelines of flood risk mapping. Beijing: Ministry of Water Resources of the People's Republic of China; 2017. Chinese.